



Cite this: *Soft Matter*, 2018, 14, 8962

Length segregation in mixtures of spherocylinders induced by imposed topological defects

Elshad Allahyarov  ^{†*abc} and Hartmut Löwen^d

We explore length segregation in binary mixtures of spherocylinders of lengths L_1 and L_2 which are tangentially confined on a spherical surface of radius R . The orientation of the spherocylinders is constrained along an externally imposed direction field on the sphere which is either along the longitude or the latitude lines of the sphere. In both situations, integer orientational defects at the poles are imposed. Using computer simulations we show that these topological defects induce a complex segregation picture also depending on the length ratio factor $\gamma = L_2/L_1$ and the total packing fraction η of the spherocylinders. When the binary mixture is aligned along the longitude lines of the sphere, shorter rods tend to accumulate at the topological defects of the polar caps whereas longer rods occupy the central equatorial area of the spherical surface. In the reverse case of latitude ordering, a new state can emerge where longer rods are predominantly both in the cap and in the equatorial areas and shorter rods are localized in between. As a reference situation, we consider a defect-free situation in the flat plane and do not find any length segregation there at similar γ and η ; hence, the segregation is purely induced by the imposed topological defects. We also develop an Onsager-like density functional theory which is capable of predicting length segregation in ordered mixtures. At low density, the results of this theory are in good agreement with the simulation data.

Received 31st August 2018,
Accepted 16th October 2018

DOI: 10.1039/c8sm01790e

rsc.li/soft-matter-journal

1 Introduction

In binary soft matter systems, segregation of different sorts of particles can occur upon a change of the thermodynamic or environmental conditions. The equivalent in bulk equilibrium thermodynamics is the phenomenon called phase separation or demixing which implies a two-phase coexistence. Whether or not phase separation occurs in the bulk for classical particles depends largely on the interactions between the particle species as well as on the temperature and the partial densities. One simple “athermal” interaction is an excluded volume (or steric) interaction between two hard bodies where temperature scales out as it only trivially sets the energy unit $k_B T$. Phase separation in binary mixtures of hard particles of different shape occurs for various combinations of shapes (see, *e.g.* ref. 1). One important and traditional example is a hard sphere mixture^{2,3} which does demix for certain size asymmetries. A further

example is a hard rod-like particle mixture which has been recently considered in various situations^{4–11} and exhibits also bulk segregation.^{12–14} Rod-like particles are more complex than spheres since they possess an additional orientational degree of freedom.

When particles are confined on a curved manifold, the segregation and phase separation are strongly affected by the underlying curvature of the configuration space. In fact, the influence of curvature on phase separation has been explored in different contexts including the crystallization transition of spheres^{15–18} and segregation in two-component vesicles.¹⁹ Phase separation was studied in curved bilayer membranes.^{20,21} A systematic analysis of the impact of curvature on phase separation was performed by computer simulations of the Widom–Rowlinson model²² and a theoretical Ginzburg–Landau approach on the sphere.²³

For rod-like particles tangentially confined to a sphere, there is not only a pure curvature effect but there are also more complex options by constraining the orientations along an imposed director field. Due to the compact topology of the sphere, a tangential director field is never defect-free but has to exhibit topological defects of the orientation.^{24–30} The two simplest cases arise if the orientation field is prescribed either along the longitude or the latitude lines of the sphere, see Fig. 1. Then, in both cases, two integer topological defects arise at the two poles. An interesting question concerns the impact of

^a Theoretische Chemie, Universität Duisburg-Essen, D-45141 Essen, Germany

^b Theoretical Department, Joint Institute for High Temperatures, Russian Academy of Sciences (IVTAN), 13/19 Izhorskaya street, Moscow 125412, Russia

^c Department of Physics, Case Western Reserve University, Cleveland, Ohio 44106-7202, USA. E-mail: elshad.allahyarov@case.edu

^d Institut für Theoretische Physik II: Weiche Materie, Heinrich-Heine Universität Düsseldorf, Universitätsstrasse 1, 40225 Düsseldorf, Germany

[†] Present address: Theoretical Chemistry, Duisburg-Essen University, Universitätsstrasse 5, 45141 Essen, Germany.

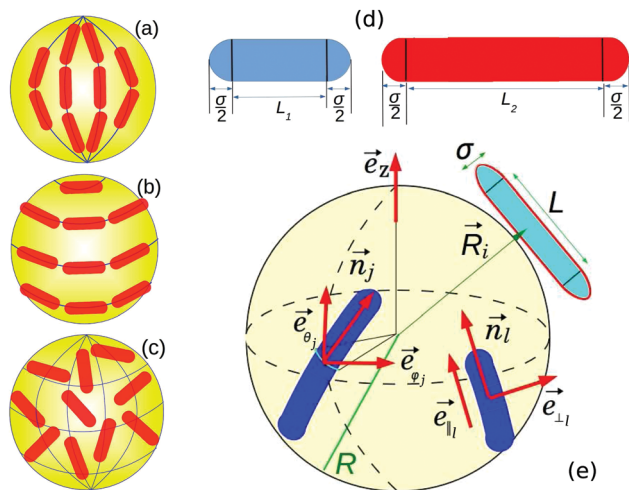


Fig. 1 Schematic pictures explaining the model. (a) A system of rods with prescribed longitude ordering; (b) a system of rods with prescribed latitude ordering; (c) a relaxed system with freely rotating rods; (d) a shorter spherocylinder of length L_1 and diameter σ , and a longer spherocylinder of length L_2 and the same diameter; (e) a spherocylinder with index i is shown as tangentially confined on a spherical surface, a spherocylinder with index j is shown to explain its orientation vector \vec{n}_j , and unit polar (\vec{e}_{θ_j}) and azimuthal (\vec{e}_{ϕ_j}) angle vectors, and a spherocylinder with index l is shown to illustrate the translational unit vectors $\vec{e}_{\perp l}$ and $\vec{e}_{\parallel l}$. The unit vector along the z -axis is denoted as \vec{e}_z .

topological defects in the constrained director field on length segregation. This is important both from a fundamental point of view since it links topology and thermodynamics and for actual applications as it enables tailoring of the segregated states on demand^{31,32} by imprinting an orientational field externally.³³

In this paper we explore the impact of imposed topological defects on segregation in binary mixtures of hard rods of different lengths by using Monte Carlo computer simulations. We confine the particles tangentially on a spherical surface and align their orientation along certain prescribed directions which possess two integer-defects at the poles. The one-component case was studied previously both at high packings³⁴ and intermediate densities³⁵ and can be used here as a reference situation. In the current study we focus on the demixing of the binary mixture on a curved surface into short-rod rich and long-rod rich zones. To our knowledge, this was never addressed in previous studies. In fact, we found that the presence of imposed defects can induce length segregation at particular values of the length ratio $\gamma = L_2/L_1$ and the total packing fraction η of the spherocylinders. When the mixture is aligned along the longitude lines of the sphere, see Fig. 1(a), shorter rods in the mixture accumulate at the polar caps of the sphere around the defects whereas longer rods occupy the equatorial area of the spherical surface. In the reverse case, when the alignment is along the latitude lines of the sphere, see Fig. 1(b), the segregation behavior becomes even richer involving in particular a state where longer rods predominantly are both in the caps around the defects and in the equatorial area, and shorter rods are localized in between. Conversely, in a reference situation of a flat plane without any

defects, there is no length segregation at similar γ and η , proving that the segregation is purely induced by the imposed topological defects.

We also propose a low-density density functional theory which is capable of predicting length segregation in ordered binary mixtures. This Onsager-like theory takes into account the excluded volumes of a rod pair in the pole area and in the equatorial area of the sphere. The difference between these excluded volumes leads to rod segregation near the poles in good agreement with our simulation data at low densities.

The remainder of this paper is structured as follows. The details of our simulation method for the spherocylinders anchored on a spherical surface are given in Section 2. Our density functional theory is described in Section 3. In Section 4 we discuss simulation results for the length segregation in binary mixtures of spherocylinders with prescribed longitude ordering. The segregation process in binary mixtures aligned along the latitude lines is analyzed in Section 5. In Section 6 we show the disappearance of the length segregation in relaxed binary mixtures. We conclude in Section 7.

2 The model

An equimolar binary mixture of hard-core spherocylinders consisting of $N/2$ rods of length L_1 and $N/2$ rods of length L_2 is anchored on a spherical surface S_2 of radius R . All rods have the same diameter σ . The end-to-end length of the spherocylinder is $L_i + \sigma$ ($i = 1, 2$), where σ accounts for the hemispherical caps at the ends of the rod, see Fig. 1(d). The rods interact through a hard-core potential

$$u_{ij}(\vec{R}_i, \vec{R}_j, \vec{n}_i, \vec{n}_j) = \begin{cases} \infty & \text{if } i \text{ and } j \text{ overlap,} \\ 0 & \text{otherwise.} \end{cases} \quad (1)$$

where the tangential unit vectors \vec{n}_i and \vec{n}_j denote the orientations of the rods i and j with anchoring positions \vec{R}_i and \vec{R}_j . The anchoring vector points from the center of the host sphere to the geometrical center of the spherocylinder, and the tangential orientation vector is directed along the long axis of the spherocylinder. These vectors are schematically shown for a single rod in Fig. 1(e). The anchoring and orientation of the i th rod are imposed by maintaining $|\vec{R}_i| = R + \sigma/2$ and $\vec{n}_i \cdot \vec{R}_i = 0$.

We consider two basic preordered configurations referred to as the longitude and latitude orderings, see Fig. 1(a) and (b). In the longitudinally ordered system, the orientation vectors \vec{n}_j of all rods are aligned along the longitudinal lines and hence they obey

$$\vec{n}_j \cdot \vec{e}_{\theta_j} = 1, \quad \vec{e}_{\theta_j} = \vec{R}_j \times (\vec{e}_z \times \vec{R}_j) \quad (2)$$

where \vec{e}_{θ_j} is the unit polar angle vector and \vec{e}_z is the unit vector along the z -axis. In a similar way, for latitude ordering, the rod orientations are fixed along the latitudinal directions in accordance with

$$\vec{n}_j \cdot \vec{e}_{\phi_j} = 1, \quad \vec{e}_{\phi_j} = (\vec{e}_z \times \vec{R}_j) \quad (3)$$

where \vec{e}_{ϕ_j} is the unit azimuthal angle vector of the j rod. All these unit vectors are schematically shown in Fig. 1(e).

As a reference situation, we also consider the case of free orientation of the rods in the absence of any further constraints except for the fact that the orientations are tangential to the spherical surface.

The total particle number density is conveniently expressed by a dimensionless areal packing fraction η . This is the ratio of all overlap-free projected rod areas (see the blue shadows in Fig. 1(e)) with respect to the full available sphere surface $4\pi R^2$.

Monte-Carlo moves were implemented for the translation and rotational moves of the rods on the spherical surface. The details of the Monte-Carlo moves are described in Appendix A.

In our calculations the packing fraction η was changed between 0.3 and 0.85, the length rate factor $\gamma = L_2/L_1$ varied between 1 and 4, and the rod length L_i was considered between 4σ and 24σ . In all simulations, the length of the shorter rod was fixed either to $L_1 = 4\sigma$ or to $L_1 = 6\sigma$. For the radius of the host sphere we consider $R = 70\sigma$. For these parameters the total number of particles N takes values between 10^3 for low density simulations and 10^4 for high density simulations.

3 Onsager-like theory for length segregation in a binary mixture

For low packing fractions, we propose a simple density functional theory to predict possible length segregation similar in mind to the approach Onsager used for the isotropic–nematic transition of a one-component rod system.³⁶ We split the full area S_2 of the sphere into two planar areas A_I and A_{II} , the former is an area enclosing the imprinted defects, and the latter is an area close to the equator where we approximate the orientational field to be constant. In order to keep the theory simple, we neglect curvature in the shape of the areas A_I and A_{II} , which is expected to work well for radii of the host sphere much larger than the rod lengths. The linear extension $\sqrt{A_I}$ of the area A_I around the defects is governed by the correlation length in the fluid at the defects which is of the order of the particle lengths while conversely the area A_{II} scales with the square of the host sphere radius R . Because of the defects, the excluded volume area $B_{ij}^{(I)}$ of a pair of rods i and j in A_I will be different from the excluded volume area $B_{ij}^{(II)}$ in A_{II} . Exact expressions for $B_{ij}^{(I)}$ and $B_{ij}^{(II)}$ are given in Appendix B.

The areas $B_{ij}^{(I)}$ for $L_1 = 6\sigma$ and $L_2 = 12\sigma$ are shown in Fig. 2 and 3 for longitude and latitude ordering, respectively. The area $B_{ij}^{(I)}$ shows a strong dependence on the ordering direction of the rods and on the choice of which rod is placed at the pole. However, the important factor here is how the areas $B_{ij}^{(I)}$ and $B_{ij}^{(II)}$ differ from each other. The latter is given by the relation

$$B_{ij}^{(II)} = 2\sigma(L_i + L_j) + \pi\sigma^2 \quad (4)$$

The ratio factor $\Gamma_{ij} = B_{ij}^{(I)}/B_{ij}^{(II)}$ for longitude ordering with shorter rod length 6σ and γ changed from 1 to 4 is always larger than one, $2.1 \leq \Gamma_{ij} \leq 9.7$. For latitude ordering, for the

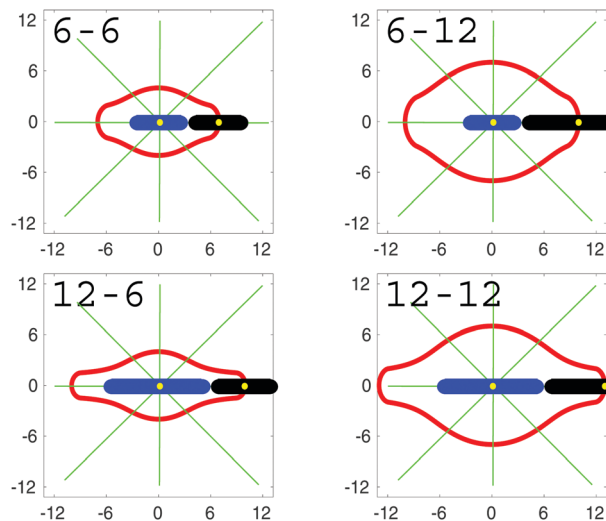


Fig. 2 The excluded volume area $B_{ij}^{(I)}$ for the two longitudinally ordered rods corresponds to the area enclosed by the red line. A mixture with $L_1 = 6\sigma$ and $L_2 = 12\sigma$ ($\gamma = 2$) is considered. The inscriptions $i - j$ ($i, j = 6, 12$) in the left top corner of the pictures indicate that the rod with length L_i is placed exactly at the pole. The red line corresponds to the distance from the pole to the center of the neighboring rod L_j . Green lines represent the possible orientations of the rod L_j . Yellow dots represent the geometrical centers of the rods. The coordinates are shown in units of σ . The ratio factor Γ_{ij} has the following values: $\Gamma_{66} = 2.95$, $\Gamma_{612} = 5.13$, $\Gamma_{126} = 2.53$, and $\Gamma_{1212} = 4.44$.

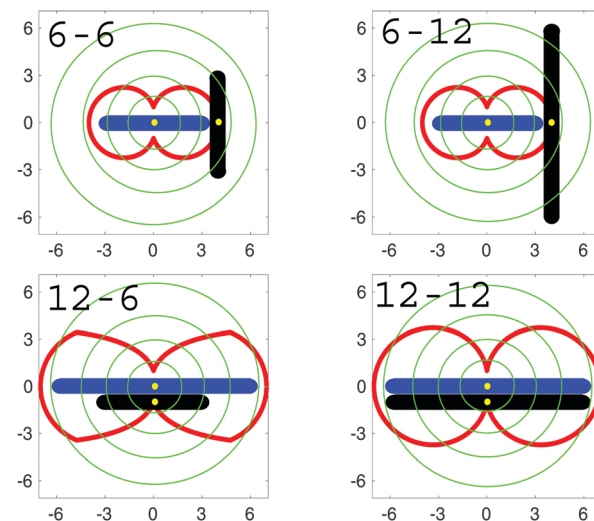


Fig. 3 Same as in Fig. 2, but now for latitude ordering. The ratio factor Γ_{ij} has the following values: $\Gamma_{66} = 1.76$, $\Gamma_{612} = 1.22$, $\Gamma_{126} = 3.11$, and $\Gamma_{1212} = 2.7$.

same binary mixture, the parameter Γ_{ij} takes values $1.2 \leq \Gamma_{ij} \leq 2.8$. Thus, in both cases the excluded volume area $B_{ij}^{(I)}$ of the rods near the poles is larger than $B_{ij}^{(II)}$. This finding has two consequences. First, in general, rods will avoid the pole area relative to the equatorial area. Second, the fact that $\Gamma_{22} > \Gamma_{11}$ implies that longer rods will tend to avoid the pole area A_I more than the shorter rods, which leads to length segregation.

More quantitatively we now construct a density functional theory from this point of view. Assuming a scaling for A_I as $\lambda_{22}B_{22}^{(I)}$ per pole (λ_{22} is defined later) such that

$$A_I = 2\lambda_{22}B_{22}^{(I)} \quad (5)$$

$$A_{II} = 4\pi R^2 - 2\lambda_{22}B_{22}^{(II)} \quad (6)$$

we consider the full system to split into two areas with densities $\rho_{I,i}$ and $\rho_{II,i}$ ($i = 1, 2$). The total density of the rods is fixed to

$$\rho_i = \frac{\rho_{I,i}A_I + \rho_{II,i}A_{II}}{A_I + A_{II}} \quad (7)$$

The total grand canonical free energy in the Onsager-like approach is then

$$\begin{aligned} \frac{\Omega}{k_B T} = & \sum_{i=1}^2 (\rho_{I,i}A_I (\ln(\rho_{I,i}A_I^2) - 1 - \mu_i) \\ & + \rho_{II,i}A_{II} (\ln(\rho_{II,i}A_{II}^2) - 1 - \mu_i)) \\ & + \frac{1}{2} \sum_{i,j=1}^2 (A_I B_{ij}^{(I)} \rho_{I,i} \rho_{I,j} + A_{II} B_{ij}^{(II)} \rho_{II,i} \rho_{II,j}) \end{aligned} \quad (8)$$

The first two terms describe the translational entropy of the rods and the last term describes repulsive interactions between the rods on the second virial coefficient level which becomes correct for low densities. A_i is the irrelevant thermal wave length and μ_i is the chemical potential to fix the prescribed density ρ_i .

Expressing $\rho_{II,i}$ from eqn (7) as

$$\rho_{II,i} = (\rho_i(A_I + A_{II}) - \rho_{I,i}A_I) \frac{1}{A_{II}} \quad (9)$$

and minimizing Ω with respect to the remaining $\rho_{I,i}$, we obtain the necessary condition $\partial\Omega/\partial\rho_{I,1} = \partial\Omega/\partial\rho_{I,2} = 0$, or explicitly

$$\begin{aligned} 0 = & A_I \ln \rho_{I,j} - A_I \ln \rho_{II,j} + A_I B_{jj}^{(I)} \rho_{I,j} \\ & + \frac{1}{2} A_I (B_{j\ell}^{(I)} + B_{\ell j}^{(I)}) \rho_{I,\ell} \\ & - A_I B_{jj}^{(II)} \rho_{II,j} - \frac{1}{2} A_I (B_{j\ell}^{(II)} + B_{\ell j}^{(II)}) \rho_{II,\ell} \end{aligned} \quad (10)$$

for $j = 1, 2$, where ℓ is the complementary index to j ($\ell = 1$ for $j = 2$ and $\ell = 2$ for $j = 1$). The two equations (10) can be solved numerically resulting in the segregation densities $\rho_{I,1}$ and $\rho_{I,2}$ at the polar area, and $\rho_{II,1}$ and $\rho_{II,2}$ (through eqn (7)) in the equator area. Note that the diameter of the host sphere enters to the DFT *via* eqn (6).

The values of the area parameter λ_{22} in eqn (5) and (6) are independent on the host sphere radius R and are fixed to 10. This corresponds to a reasonable correlation length.

4 Demixing in a binary mixture with longitudinal ordering

We first start with the binary mixture aligned along the longitude lines of the spherical surface S_2 , see Fig. 1(a). The state

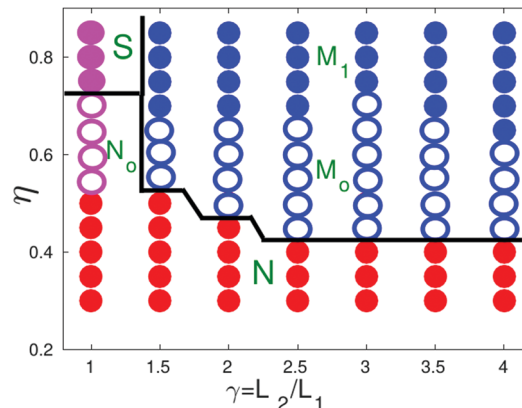


Fig. 4 State diagram for the binary mixture of rods with prescribed longitude ordering. Black lines are guides for the eye to separate smectic S and nematic N_0 states from the segregation structures M_1 , M_0 . The nematic state N shows very weak segregation behavior.

diagram of the simulated structures corresponding to this ordering with representative snapshots and schematic pictures are shown in Fig. 4 and 5. In the latter, shorter rods are colored blue, while the coloring of longer rods depends on the nematic ordering in their surroundings. Yellow colored longer rods have less nematic ordering than dark red colored rods. Corresponding plots for the normalized polar densities of rods

$$\rho_i(\theta) = \frac{2}{N} \frac{n_i(\theta)}{\cos(\theta) - \cos(\theta + \Delta\theta)} \quad (11)$$

where $i = 1, 2$ for shorter and longer rods, respectively, are shown in Fig. 6. Here $n_i(\theta)$ is the number of rods inside the strip area enclosed by the latitude lines θ and $\theta + \Delta\theta$, and a bin width $\Delta\theta = \pi/20$ was used in simulations.

The state diagram in Fig. 4 distinguishes five different states possible for the binary mixture of rods as a function of η and γ . For the monodisperse system, the stable low-density nematic phase N is followed by a medium-density nematic phase N_0 with a depleted density in the equatorial zones and a high-density smectic phase S. These states were discussed in ref. 35 and are just shown here as a reference case, see black lines in Fig. 6.

Obviously, for the mixture, at low-density a nematic phase N is stable. A representative snapshot and schematic picture for this state are provided in the third row of Fig. 5. In this state the distribution of the shorter rods for all γ is almost homogeneous on S_2 , $\rho_1(\theta) \approx 1$. For larger $\gamma \geq 2$ cases a clustering in the longer particles develops. Comparison of $\rho_1(\theta)$ and $\rho_2(\theta)$ for this state does not show any robust demixing except a slight deficiency of longer rods at the poles. This is schematically depicted in the third row of Fig. 5.

Upon increasing the density there are two further states in Fig. 4, denoted as M_0 for medium density and M_1 for high density mixtures, which show clear length segregation properties. The letter M in these notations refers to the rod alignment in the segregated states along the ‘meridian’-lines of the host sphere. In both states the shorter rods are accumulating near the poles followed by a zone enriched with longer rods, see the yellow and

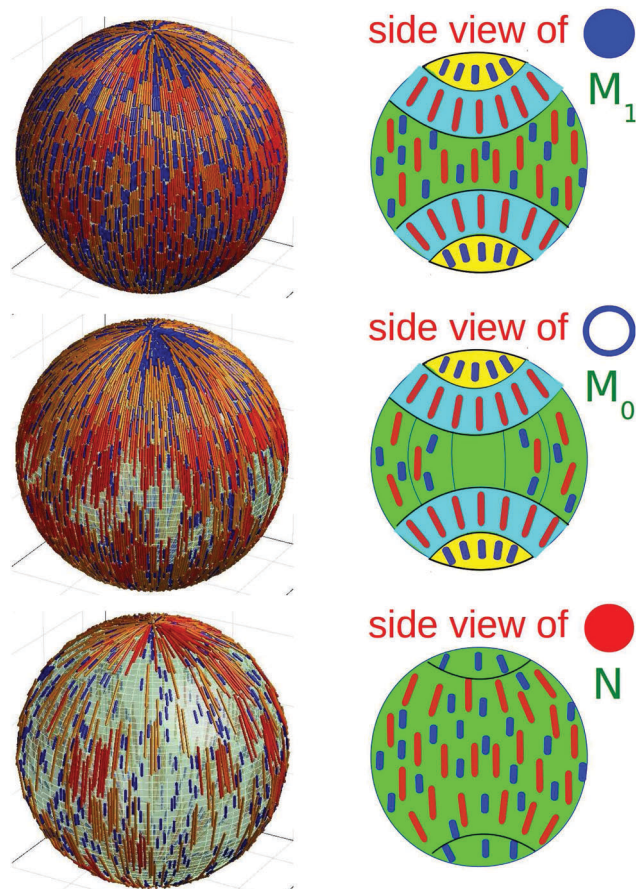


Fig. 5 Simulation snapshots and schematic pictures for the three representative structures from Fig. 4. In the snapshots shorter rods are colored blue. The coloring of longer rods, from yellow to dark red, corresponds to the strength of nematic ordering in their surroundings. In the right column, the places preferably occupied by one sort of rod are colored differently. Moreover, for the polar area a yellow color, for the central area a green color, and for the area in between a cyan color are used. In the M_0 and M_1 states, the yellow and cyan colored areas correspond to the shorter rod rich and longer rod rich areas, respectively. The empty green colored area in M_0 corresponds to the void-like spaces. In the states M_1 , M_0 , and N the same colored area filled with shorter and longer rods corresponds to a homogeneous distribution of partial densities.

cyan colored areas in Fig. 5. The difference between M_0 and M_1 is that there are void-like spaces in the equatorial area for M_0 which gradually vanish for M_1 . The formation of the different zones is visible and quantified in plots of the partial densities in Fig. 6. In particular, the longer particles exhibit a double maximum on S_2 . The segregation strength is higher at $\eta = 0.5$ for the medium-density M_0 state as compared to the high-density state M_1 . At the same time, below $\eta < 0.4$ the segregation also weakens.

Finally, it should be noted that the length segregation in the M_1 and M_0 states stems exclusively from the topological defects imposed on the host surface S_2 . This is proved by the inability of a planar defect-free surface to keep the initially segregated structure of the mixture intact, see the results of our additional simulations presented in Appendix C.

We now compare simulation results against our density functional theory (DFT) for low densities where the DFT is

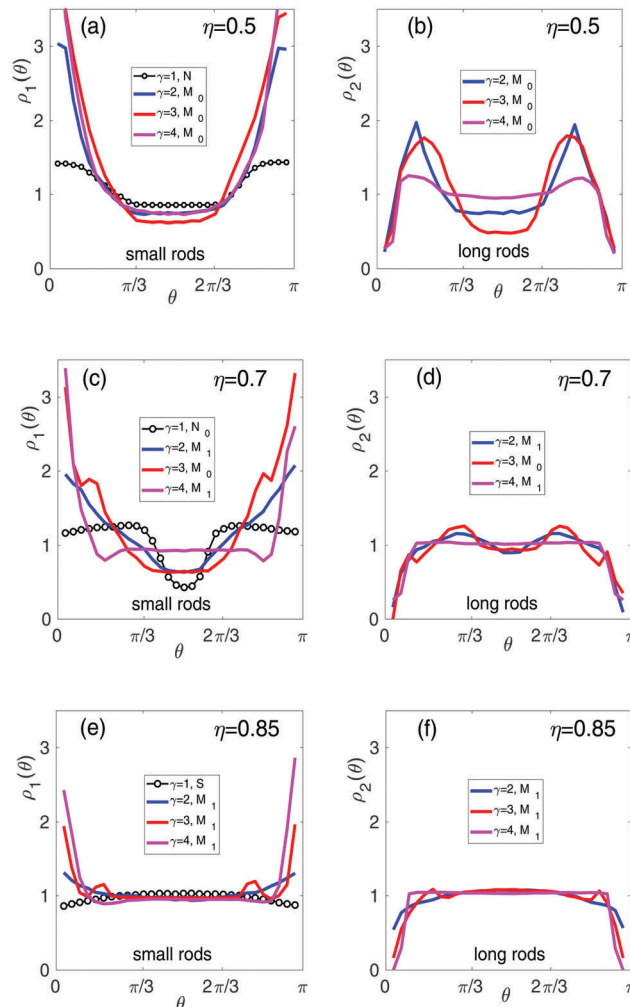


Fig. 6 Longitudinally ordered binary mixture with the shorter rod length $L_1 = 6\sigma$. Cases (a), (c) and (e): normalized polar density $\rho_1(\theta)$ for the shorter rods. Cases (b), (d) and (f): normalized polar density $\rho_2(\theta)$ for the longer rods. Black line with symbols – $\gamma = 1$, blue line – $\gamma = 2$, red line – $\gamma = 3$, pink line – $\gamma = 4$. The corresponding packing fractions η and the states of the mixture from Fig. 4 are given as insets in the figures.

expected to perform well. Due to the division of areas into two parts, the partial density profiles are simple sharp-kink functions. Fig. 7a reveals that the DFT predictions are in agreement with the simulation data both qualitatively and quantitatively for the low density $\eta = 0.1$, and $L_1 = 6\sigma$, $\gamma = 3$. In particular, the density of rods is lower at the poles than in the equatorial area and longer rods are more depleted around the poles. Hence the theory describes the segregation behavior pretty well.

A direct comparison between the simulated rod densities, averaged over the area A_k ($k = I, II$),

$$\rho_{k,i} = \frac{1}{\Theta_k} \int_{\Theta_k} \rho_i(\theta) d\theta \quad (12)$$

and the DFT results is given in Fig. 7b. Fig. 7b shows that the segregation trend as a function of length ratio γ is correctly reproduced by the theory.

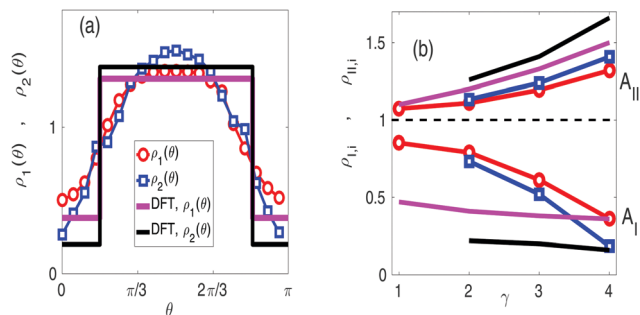


Fig. 7 Rod densities for longitudinal ordering with $\eta = 0.1$, $L_1 = 6\sigma$ and different γ . (a) $\gamma = 3$, red line with circles – simulation data for the density $\rho_1(\theta)$ of shorter rods, blue line with squares – simulation data for the density $\rho_2(\theta)$ of longer rods, pink full line – DFT prediction for the density $\rho_1(\theta)$ of shorter rods, black full line – DFT prediction for the density $\rho_2(\theta)$ of longer rods. (b) γ is changed from 1 to 4, the curves correspond to the partial rod densities $\rho_{j,i}$ of species $i = 1, 2$ in the areas A_j ($j = I, II$). All data for A_I (A_{II}) are below (above) the unity line. Red lines with circles – simulation data for shorter rods, blue lines with squares – simulation data for longer rods, pink lines – DFT prediction for shorter rods, black lines – DFT prediction for longer rods.

5 Demixing in a binary mixture with latitude ordering

Now we turn to latitudinal ordering. The state diagram, representative snapshots and schematic pictures are presented in Fig. 8 and 9. Corresponding plots for the polar particle densities $\rho_1(\theta)$ and $\rho_2(\theta)$ are shown in Fig. 10.

A length segregated structure E_0 is shown schematically in the first row of Fig. 9. The letter E in this notation refers to the rod alignment along the ‘equator’-lines of the host sphere. In this state shorter rods accumulate near the edges of the empty cap, and the longer rods occupy the central area of S_2 . The blue, red, and pink lines in the first row pictures, and the blue and red lines on the second row pictures of Fig. 10 correspond to the particle densities of this state.

The occurrence of bald polar patches in E_0 is basically associated with the higher bending energy of the nematic

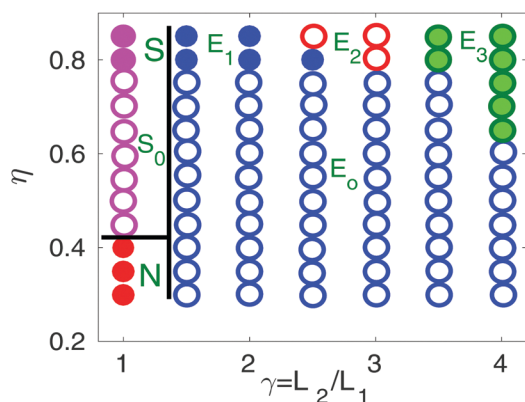


Fig. 8 State diagram for a binary mixture of rods with prescribed latitude ordering. Data for a one-component system with $\gamma = 1$ are given as a reference. Black lines separate smectic S and S_0 , and the nematic N states from the segregated structures.

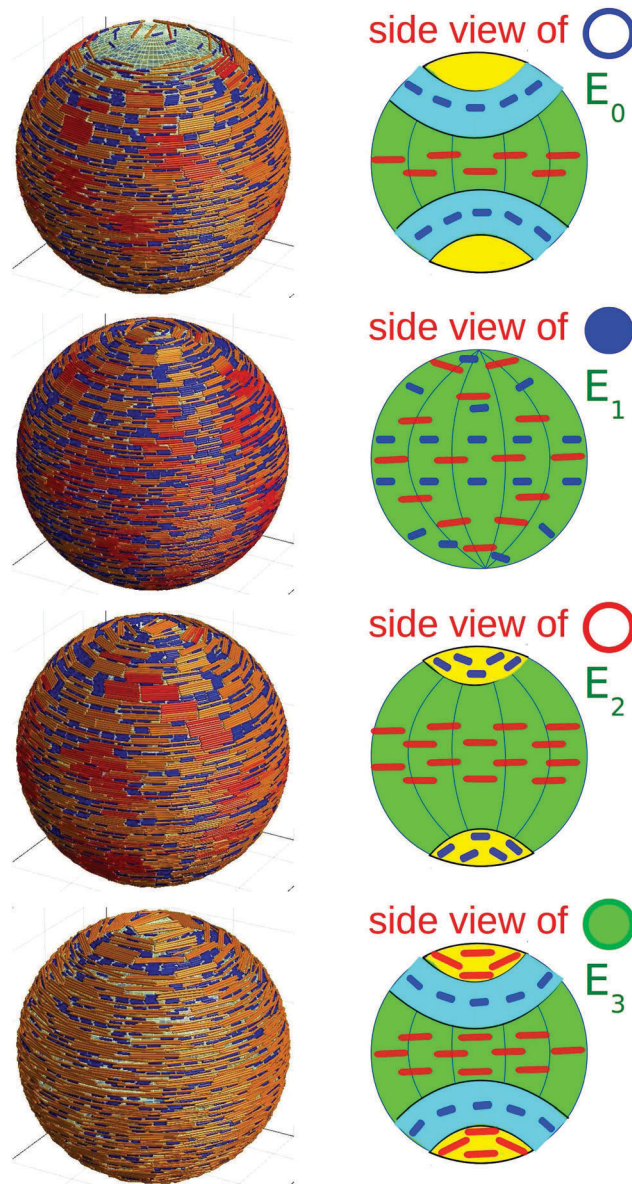


Fig. 9 Same as Fig. 5 but now for latitude ordering: simulation snapshots and schematic pictures for the four representative structures from Fig. 8. In the state E_0 the yellow color corresponds to an empty area, the cyan color corresponds to the area mostly occupied by shorter rods, and the green color corresponds to the area where the longer rods prevail. In the state E_1 the green color covering the entire surface S_2 exhibits the homogeneous distribution of all rods. In the state E_2 the yellow color corresponds to the area mostly occupied by shorter rods, and the green color corresponds to the area where longer rods prevail. In the state E_3 the yellow color corresponds to the area where longer rods prevail, the cyan color corresponds to the area mostly occupied by shorter rods, and the green color in the central area points to the abundance of longer rods there.

director near the poles. This energy is proportional to $L_i/(R \sin(\theta))$ ($i = 1, 2$) and thus is larger near the poles where $\sin(\theta)$ is very small. For this reason both the shorter and longer rods avoid the poles but the deficiency is more pronounced for longer rods.

At high packing fractions the E_0 segregation state transfers either to a weakly segregated state E_1 at low γ , or to a

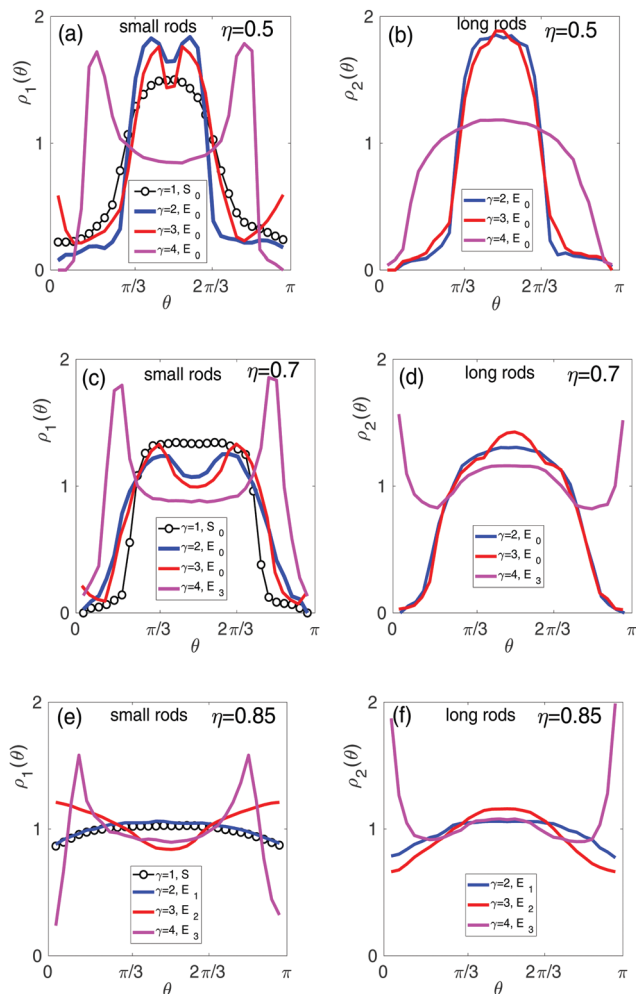


Fig. 10 Latitude ordered binary mixture with the shorter rod length $L_1 = 6\sigma$. Cases (a), (c) and (e): normalized polar density $\rho_1(\theta)$ for the shorter rods. Cases (b), (d) and (f): normalized polar density $\rho_2(\theta)$ for the longer rods. Black line with symbols – $\gamma = 1$, blue line – $\gamma = 2$, red line – $\gamma = 3$, pink line – $\gamma = 4$. The corresponding packing fractions η and the states of the mixture from Fig. 8 are given as insets in the figures.

moderately segregated state E_2 at the moderate values of γ , or to a strongly segregated state E_3 at the high values of γ .

The weakly segregated state E_1 , shown in the second row of Fig. 9, has a weak avoidance of poles for both species as seen from the blue curves in Fig. 10(e) and (f). This effect can be also explained by the higher values of the bending energy at the poles. Although there are slightly more shorter rods at the poles compared to the longer rods, in the schematic picture of this state in Fig. 9 we show a homogeneous distribution for the rods.

In the moderately segregated state E_2 , shown in the third row of Fig. 9, more shorter rods accumulate at the poles and more longer rods fill in the central area of S_2 . This is evident from the red lines in the third row picture of Fig. 10. Again, qualitatively, this picture can be explained by the higher bending values for longer rods compared to the bending energy of shorter rods.

The most intriguing state in the latitude ordered mixture is the segregated state E_3 which is shown in the fourth line of Fig. 9.

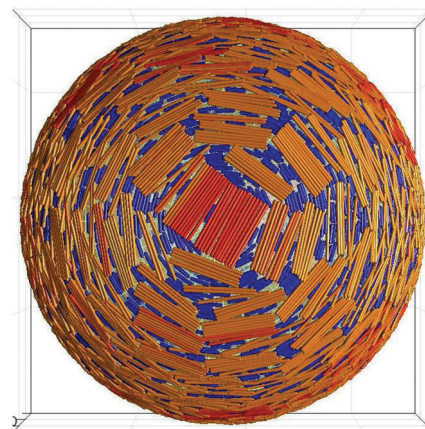


Fig. 11 Top view snapshot corresponding to the state E_3 for latitude ordering with parameters $L_1 = 6\sigma$, $\gamma = 4$ and $\eta = 0.8$. Clearly the polar region is basically occupied by longer rods.

In this state the longer rods mostly exhibit a double occupation tendency: they outnumber the shorter rods at the poles and in the central area of S_2 . As a result, the shorter rods are sandwiched between these areas. This unique segregation picture appears only at high packing fractions $\eta \geq 0.6$ and high values of length ratio factor $\gamma \geq 3.5$. The prevalence of longer rods in the polar region can be understood in the following manner. As can be seen from the top view snapshot in Fig. 11 for the mixture with $L_1 = 6\sigma$, $\gamma = 4$ and $\eta = 0.8$, the longer rods form a big cluster across the pole. If we assume that the cluster accommodates N_2 longer rods, it is obvious to expect that $N_1 = \gamma N_2$ shorter rods will be needed otherwise to cover the same area. However, because of the ordering constraint, the shorter rods will have a mismatch between their mutual orientations in this area. The more angular mismatches there are between the rods, the less the packing of the polar zone by the rods. Therefore, longer rods, which are capable of building larger and ordered clusters across the pole without violating their prescribed ordering, will be more effective to pack the polar area.

Finally we compare again our DFT to the simulation data at low density with $\eta = 0.1$, $L_1 = 6\sigma$, and $\gamma = 3$, see Fig. 12. Similar as for latitude ordering, the partial density profiles compare well with the simulation data and all trends are reproduced except for an ordered shell in the density profile (visible in the simulation data in Fig. 12a) which arises from finite density.

In Fig. 12b we directly compare the averaged rod densities $\rho_{k,i}$ with the theoretical predictions, $k = \text{I, II}$ and $i = 1, 2$. Here, again, the lines below (above) the unity line correspond to the rod densities in the area A_1 (A_{II}). In total, Fig. 12b strongly resembles Fig. 7b: the angular and length segregation effects become stronger at higher values of γ , and the DFT theory prediction overestimates these effects in the binary mixture. However, compared to the longitude ordered case considered in Fig. 7b, now the DFT theory provides quite good agreement with the simulations, especially at higher γ .

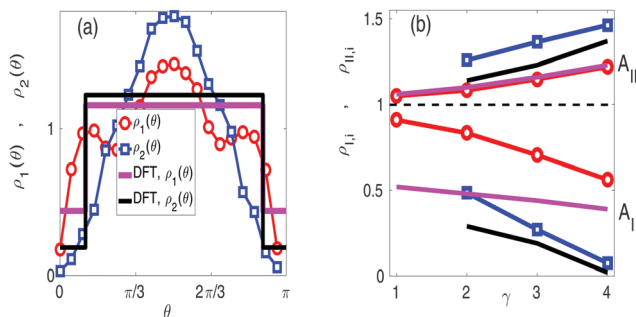


Fig. 12 Comparison between theory (DFT) and simulation results for latitude ordering with $\eta = 0.1$, $L_1 = 6\sigma$ and different γ . All line descriptions are the same as in Fig. 7.

6 Loss of segregation in freely rotating binary mixtures

When the angular constraints are taken off and the rods are given the freedom to rotate around their radius vectors \vec{R}_i , the length segregation ability of the states is lost completely for the cases when $\gamma < 4$. This can be evidenced from the snapshot pictures shown in Fig. 13 where the relaxed states of the initially longitude and latitude ordered configurations are examined. The left column pictures in this figure correspond to the ordered state, whereas the right column pictures are for the freely rotated state. Whereas the imposed defects at the pole are lost, few other topological defects on the particle scale

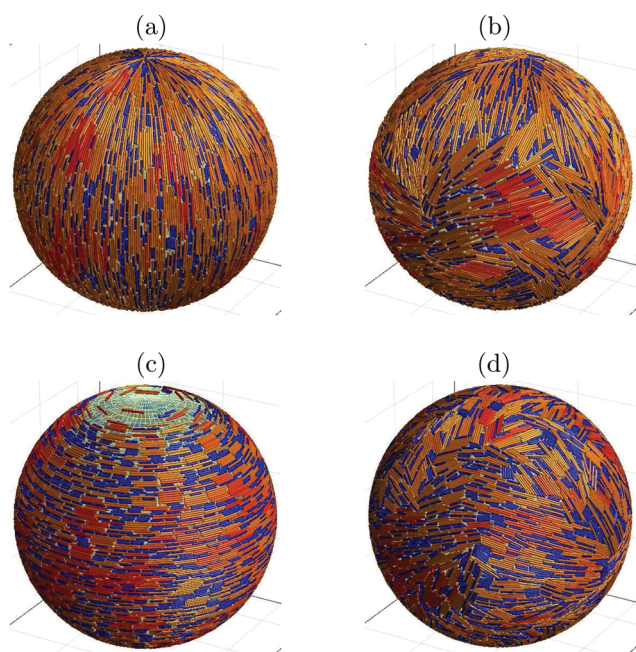


Fig. 13 Case (a): a state with longitude ordering for $L_1 = 6\sigma$, $\gamma = 3$ and $\eta = 0.85$ corresponding to the segregation structure M_1 ; case (b): corresponding freely rotated state with no angular constraints. Case (c): a state with latitude ordering for $L_1 = 6\sigma$, $\gamma = 2$ and $\eta = 0.7$ corresponding to the segregation structure E_0 ; case (d): corresponding freely rotated state with no angular constraints.

emerge elsewhere on S_2 . As a consequence, the length segregation effect in the mixture is completely destroyed.

Furthermore, our simulations reveal that the total equilibration of freely rotated systems with $\gamma = 4$ and $\eta > 0.5$ suffers from the jamming of longer rods. Interestingly, if the binary mixture is replaced by a monodisperse system consisting of only the longer rods, no such jamming issue is encountered. For example, a system with $L_1 = L_2 = 24\sigma$ and $\eta = 0.7$ will quickly lose its initial orientation when the prescribed ordering field is taken off, see Appendix D for details. Thus, the free rotation of shorter rods creates an additional obstacle to the relaxation of longer rods in the binary mixture.

7 Conclusions

In conclusion, we report on the length segregation in an aligned binary mixture of monodisperse spherocylinders induced by orientational topological defects imposed on the host surface. We have shown that an ordered binary mixture on a curved host surface is inclined to demix into short-rod rich and long-rod rich zones depending on the length ratio parameter γ and the packing fraction η of the spherocylinders. In longitudinally aligned binary mixtures, shorter rods are in abundance at the polar caps of the sphere whereas longer rods accumulate in the equatorial area of the spherical surface. For the binary mixture with prescribed latitude ordering the segregation becomes more complex. We detected a process when longer rods are predominant both in the cap and in the equatorial areas and shorter rods are localized in between.

Our simulations also show that the length segregation is only possible in the preordered states and completely disappears in the freely rotated state. Moreover, all simulations reported here were limited to symmetrical mixtures with the mixing ratio $N_1/N_2 = 1$. This choice is dictated by our aim to focus on the role played by the length ratio parameter γ in the segregation of binary mixtures but similar segregation scenarios are expected for mixtures which are not exactly equimolar.

An interesting question to answer will be how the segregation process depends on the radius of the host surface, or, more specifically, on the aspect ratios L_1/R and L_2/R . On the one hand, for smaller radius R of the S_2 the segregation is expected to become stronger, however, in this case the density fluctuations in the mixture with a low number of particles will blur the segregation picture. In fact, our test simulations for a smaller sphere with radius $R = 40\sigma$ confirmed that the observed segregation picture is qualitatively similar to the results discussed here, however the noise in the density fluctuations obscures the details of the segregation. On the other hand, for larger R , in the limit of approaching the flat surface case, no length segregation is expected as seen from Appendix C except near the poles.

We believe that our study will attract more refined density functional theories valid at higher densities. Fundamental measure density functional theory is one of the promising tools for such microscopic theories as it was applied to hard spherocylinders and rectangles confined on two-dimensional

flat and curved manifolds even with orientational constraints.^{37,38} Moreover it would be interesting to see how stable the segregation effect will be if the simulation model is changed in terms of interactions and set-ups.^{16,39–43} Last it is worth pointing out that active particles have been studied on the sphere revealing phenomena like swarm winding,^{44–46} aging⁴⁷ and topological sound creation⁴⁸ but length segregation is still unexplored in active systems in the presence of defects.

Finally we emphasize that the segregation behavior predicted by our simulations can in principle be verified with experiments using smectic shells of molecular crystals^{49–58} or Pickering emulsion droplets covered with rod-like colloids.^{59–64} Another option is layers of silica rods which have been recently studied under various constraints,^{65,66} aspherical surfactants⁶⁷ or ellipsoidal colloids bound to curved fluid–fluid interfaces.⁶⁸ Even living and motile “particles” like cells⁴¹ and rod-like fly embryos⁶⁹ were recently studied on spheres. An orientational constraint can be imprinted by using external fields or a molecular liquid crystal which prescribes the orientational ordering of larger colloidal rods.³³

Conflicts of interest

There are no conflicts to declare.

Appendix

A Monte-Carlo moves for the rods on spherical surface

Monte-Carlo translational displacements were done by randomly choosing a rod j , $j = 1, \dots, N$, and attempting to move it from its current position \vec{R}_j to a new position \vec{R}_j^{new} on the host sphere. These moves are then followed by the rotational moves of the rod orientations. For the preordered configurations the rotational move is done to keep the particle orientation fixed according the angular constraints given by eqn (2) and (3). For the freely rotated state without angular constraints for the rod orientation, the rotational moves consist of randomly choosing a rod orientation. In order to speed up the system equilibration, the Monte-Carlo translational moves are carried within a spherical cap around the particle position \vec{R}_j with angular opening ψ and, therefore, with maximal displacement length $d_{\text{MC}} = (R + \sigma/2)\psi$ fixed to $d_{\text{MC}} = 3\sigma$.

For generating a new position \vec{R}_j^{new} for the j th rod, the following three steps are taken in a consecutive manner. First, a random point \vec{a}_1 is generated around the north pole of the unit sphere within a cap with angular opening ψ . The components of \vec{a}_1 are defined as

$$\begin{aligned} \xi &= 2\pi\zeta_1 \\ \chi &= \arccos(1 - (1 - \cos\psi)\zeta_2) \\ a_{1x} &= \sin\chi \cos\xi \\ a_{1y} &= \sin\chi \sin\xi \\ a_{1z} &= \cos\chi \end{aligned} \quad (\text{A1})$$

where ζ_1 and ζ_2 denote random numbers uniformly distributed in the interval $[0,1]$. Second, the vector \vec{a}_1 rotated around the axis \vec{x} by the azimuthal angle θ_j of rod j . The resulting position \vec{a}_2 is given as

$$\begin{aligned} a_{2x} &= a_{1x} \\ a_{2y} &= a_{1y} \cos\theta_j - a_{1z} \sin\theta_j \\ a_{2z} &= a_{1y} \sin\theta_j + a_{1z} \cos\theta_j \end{aligned} \quad (\text{A2})$$

Third, the vector \vec{a}_2 rotated around the axis \vec{z} by the polar angle φ_j of rod j . The components of the resulting position \vec{a}_3 are

$$\begin{aligned} a_{3x} &= a_{2x} \cos\varphi_j - a_{2y} \sin\varphi_j \\ a_{3y} &= a_{2x} \sin\varphi_j + a_{2y} \cos\varphi_j \\ a_{3z} &= a_{2z} \end{aligned} \quad (\text{A3})$$

Finally, the position $(R + \sigma/2)\vec{a}_3$ is taken as the new displacement point \vec{R}_j^{new} for the rod j . Obviously, \vec{R}_j^{new} lies within a spherical cap with opening ψ around the rod position \vec{R}_j .

After the j th rod's Monte-Carlo translational displacement, its orientation \vec{n}_j is adjusted in order to fulfill the preordered longitude or latitude conditions at the new position according to eqn (2) and (3), respectively.

After the translational and orientational steps, the new position for the j th rod is accepted if there is no mutual overlap of rods.⁷⁰ In the opposite case, the particle is kept at its old anchoring position \vec{R}_j .

The system is equilibrated during 10^7 – 10^8 Monte-Carlo steps per particle comprising translational moves followed by the adjusting steps to \vec{n}_j for the system particles $j = 1, \dots, N$. In the following the same number of simulation steps was used to gather statistics for the production phase.

Each initial configuration with packing fraction η was created by one-by-one insertion of rods (for the two species) at random positions on S_2 under the imposed angular constraint for their orientation. At the random insertion point \vec{R}_j , the corresponding angular vectors \vec{e}_{θ_j} and \vec{e}_{φ_j} were defined to get the correct orientation for the j th rod. If the inserted j th rod overlaps with one of the $j - 1$ rods successfully inserted before it, more insertion attempts are done for the j th rod until its insertion is successful. Starting from $\eta > 0.35$, however, the insertion step becomes less productive because of the increased rate of overlappings with the rods inserted on S_2 before. This issue is effectively solved by allowing all other $j - 1$ particles to take Monte-Carlo moves on S_2 .³⁵ During these moves each rod i , $1 \leq i \leq j - 1$, first takes a translational move followed by the adjustment step to its orientation \vec{n}_i to fulfill the preordering conditions, eqn (2) and (3) for the longitude and latitude orderings, respectively.

Finally, initial configurations for the freely oriented configurations were obtained by relaxing the completed simulations for the preordered mixtures, *i.e.* by lifting the imposed angular restriction. This gives each particle i , $1 \leq i \leq N$, the ability to freely rotate around its radius-vectors \vec{R}_i , see Fig. 1(c).

B Excluded volume of ordered and binary rods B_{ij}^I at the pole

The excluded volume area B_{ij}^I for a pair of rods with longitude ordering in the polar region A_I can be calculated as the area enclosed by the parametric curve

$$x(\beta) = \frac{L_i}{2} + \sigma \cos(\kappa(\beta)) + \frac{L_j}{2} \cos(\beta) \quad (\text{B1})$$

$$|y(\beta)| = \sigma \sin(\kappa(\beta)) + \frac{L_j}{2} \sin(\beta)$$

for $0 \leq \beta \leq \beta_{\min}$ and $\pi - \beta_{\min} \leq \beta \leq \pi$, and

$$x(\beta) = \frac{\sigma}{\tan(\beta)} + \frac{L_j}{2} \cos(\beta) \quad (\text{B2})$$

$$|y(\beta)| = \sigma + \frac{L_j}{2} \sin(\beta)$$

for $\beta_{\min} < \beta < \pi - \beta_{\min}$, where β_{\min} depends on the length L_i of the rod i , $\beta_{\min} = 2\sigma/L_i$. Here the angle $\kappa(\beta)$ depends on the parametric angle β through the transcendental equation

$$\tan(\beta) = \frac{2\sigma \sin(\kappa(\beta))}{L_i + 2\sigma \cos(\kappa(\beta))} \quad (\text{B3})$$

eqn (B1) and (B2) are derived for the case when the rod i is placed at the pole and is surrounded by the rods j . The coordinates $(x(\beta), y(\beta))$ of the parametric curve define the distance $r(\beta) = \sqrt{x(\beta)^2 + y(\beta)^2}$ between the centers of the rods i and j .

The corresponding parametric curve for the excluded volume area B_{ij}^I of latitude ordered rods in the polar region A_I are described as

$$x(\beta) = \left(\sigma + \frac{L_i}{2} \cos(\beta) \right) \cos(\beta) \quad (\text{B4})$$

$$|y(\beta)| = \left(\sigma + \frac{L_i}{2} \cos(\beta) \right) \sin(\beta)$$

for $0 \leq \beta \leq \beta_{\min}$ and $\pi - \beta_{\min} \leq \beta \leq \pi$, and

$$x(\beta) = \left(\sigma + \frac{L_j}{2} \cos(\beta) \right) \frac{\cos(\beta)}{\sin(\beta)} \quad (\text{B5})$$

$$|y(\beta)| = \sigma + \frac{L_j}{2} \cos(\beta)$$

for $\beta_{\min} < \beta < \pi - \beta_{\min}$. Here β_{\min} depends on the lengths of both rods, L_i and L_j , and is defined as the solution of the following transcendental equation,

$$L_j \cos(\beta_{\min}) + 2\sigma = \sin(\beta_{\min})(L_i \cos(\beta_{\min}) + 2\sigma) \quad (\text{B6})$$

and eqn (B4) and (B5) are derived for the case when the rod i is placed at the pole and is surrounded by the rods j . Here again the coordinates $(x(\beta), y(\beta))$ of the parametric curve define the distance $r(\beta) = \sqrt{x(\beta)^2 + y(\beta)^2}$ between the centers of the rods i and j .

Once the coordinates $x(\beta)$ and $y(\beta)$ of the parametric curve are established, the excluded volume area B_{ij}^I in the region A_I

can be calculated as the area under the parametric curve,

$$B_{ij}^I = 2 \int_0^\pi y(\beta) \frac{dx(\beta)}{d\beta} d\beta \quad (\text{B7})$$

Equivalently, the area under the parametric curve can be calculated numerically.

C Oriented binary mixture on a flat surface

In order to show that the length segregation in the aligned binary mixture is only possible on curved surfaces, we ran three additional simulations with different length ratios on a flat surface with initially segregated mixtures. The snapshots for the fully segregated mixtures at the simulation time $t = 0$ with the length ratio factors $\gamma = 2, 3$, and 4 at the mixture composition 0.5 and the packing fraction $\eta = 0.7$ are shown in the left column of Fig. 14. The completely mixed configurations shown in the right column correspond to the simulation results after 10^6 Monte-Carlo steps. The linear densities of the shorter and longer rods along any direction show a homogeneous distribution of particles with no length segregation.

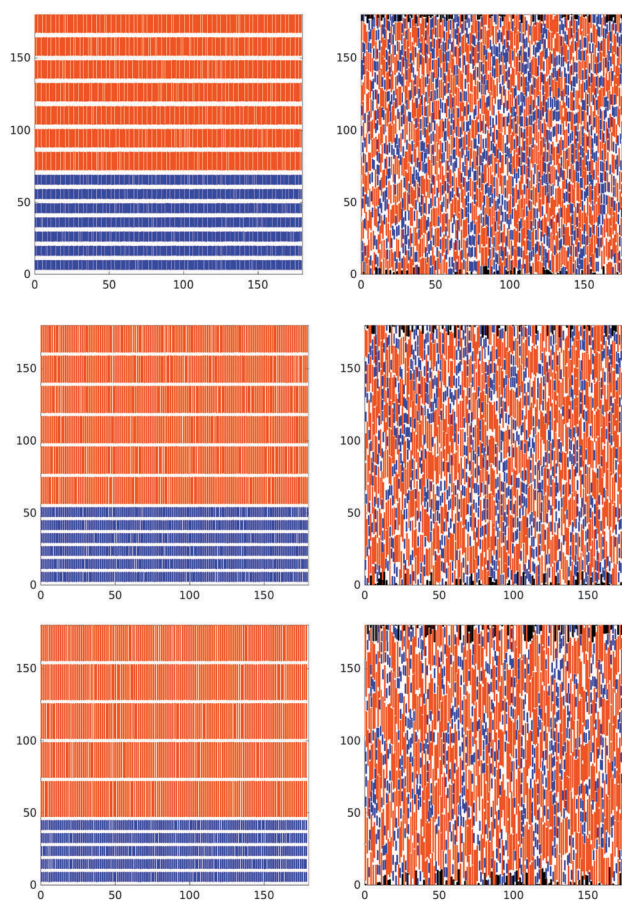


Fig. 14 Simulations of the ordered binary mixture on a flat surface. Left column – initial configuration with sharply segregated state. Right column – equilibrated state in which the initial segregation is lost. The system parameters are: $L_1 = 6\sigma$, $\eta = 0.7$. First row – $\gamma = 2$. Second row – $\gamma = 3$. Third row – $\gamma = 4$.

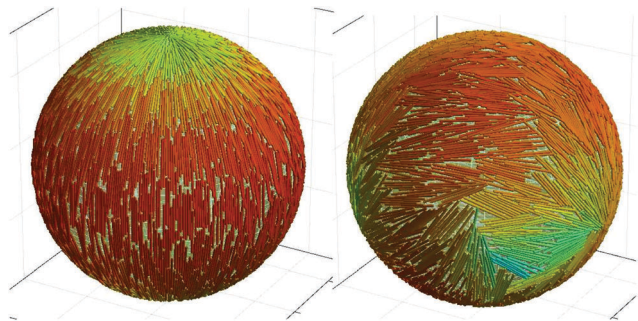


Fig. 15 Simulation snapshots for a monodisperse system of spherocylinders with $L = 24\sigma$ and $\eta = 0.7$. Left picture – a system with prescribed longitudinal ordering. Right picture – freely rotated system.

D Loss of ordering in a one-component system of longer rods

We ran a one-component (monodisperse) $L_1 = L_2 = 24\sigma$ system simulation at $\eta = 0.7$ without the shorter rods. The snapshots presented in Fig. 15 indicate that the system loses its initial ordering in the freely rotated state.

Acknowledgements

We thank A. Voigt for helpful discussions. We acknowledge support of this work by the Deutsche Forschungsgemeinschaft (DFG) through the grants AL 2058/1-1 (for E. A.) and LO 418/20-1 (for H. L.).

References

- R. van Roij and B. Mulder, *Phys. Rev. E: Stat. Phys., Plasmas, Fluids, Relat. Interdiscip. Top.*, 1996, **54**, 6430–6440.
- M. Dijkstra, R. van Roij and R. Evans, *Phys. Rev. E: Stat. Phys., Plasmas, Fluids, Relat. Interdiscip. Top.*, 1999, **59**, 5744–5771.
- M. M. H. D. Arntz, H. H. Beefink, W. K. den Otter, W. J. Briels and R. M. Boom, *AIChE J.*, 2014, **60**, 50–59.
- A. M. Bohle, R. Holyst and T. Vilgis, *Phys. Rev. Lett.*, 1996, **76**, 1396–1399.
- G. Cinacchi, L. Mederos and E. Velasco, *J. Chem. Phys.*, 2004, **121**, 3854–3863.
- Y. Martinez-Raton, E. Velasco and L. Mederos, *J. Chem. Phys.*, 2005, **123**, 104906.
- S. Varga, E. Velasco and L. Mederos, *et al.*, *Mol. Phys.*, 2009, **107**, 2481–2492.
- D. de las Heras, Y. Martinez-Raton and E. Velasco, *Phys. Rev. E: Stat., Nonlinear, Soft Matter Phys.*, 2010, **81**, 021706.
- T. Schilling, S. Dorosz and M. Radu, *et al.*, *Eur. Phys. J.: Spec. Top.*, 2013, **222**, 3039–3052.
- R. Lugo-Frias and S. H. L. Klapp, *J. Phys.: Condens. Matter*, 2016, **28**, 244022.
- M. Testa-Anta, M. A. Correa-Duarte and V. Salgueirino, *Part. Part. Syst. Charact.*, 2018, **35**, 1800046.
- S. Varga, A. Galindo and G. Jackson, *Phys. Rev. E: Stat., Nonlinear, Soft Matter Phys.*, 2002, **66**, 011707.
- S. Calus, B. Jablonska, M. Busch, D. Rau, P. Huber and A. V. Kityk, *Phys. Rev. E: Stat., Nonlinear, Soft Matter Phys.*, 2014, **89**, 062501.
- J. Kundu, J. F. Stilck and R. Rajesh, *Europhys. Lett.*, 2015, **112**, 66002.
- R. Backofen, A. Voigt and T. Witkowski, *Phys. Rev. E: Stat., Nonlinear, Soft Matter Phys.*, 2010, **81**, 025701.
- S. Paquay, G. J. Both and P. van der Schoot, *Phys. Rev. E*, 2017, **96**, 012611.
- C. Koehler, R. Backofen and A. Voigt, *Phys. Rev. Lett.*, 2016, **116**, 135502.
- R. E. Guerra, C. P. Kelleher, A. D. Hollingsworth and P. M. Chaikin, *Nature*, 2018, **554**, 346–350.
- U. Seifert, *Phys. Rev. Lett.*, 1993, **70**, 1335–1338.
- R. Parthasarathy, C.-H. Yu and J. T. Groves, *Langmuir*, 2006, **22**, 5095–5099.
- Y. Li, R. Lipowsky and R. Dimova, *Proc. Natl. Acad. Sci. U. S. A.*, 2011, **22**, 4731–4736.
- T. Fischer and R. L. C. Vink, *J. Phys.: Condens. Matter*, 2010, **22**, 104123.
- M. C. Bott and J. M. Brader, *Phys. Rev. E*, 2016, **94**, 012603.
- P. M. Chaikin and T. C. Lubensky, *Principles of Condensed Matter Physics*, Cambridge University Press, 1995.
- D. R. Nelson, *Defects and Geometry in Condensed Matter Physics*, Cambridge University Press, 2002.
- P. G. de Gennes and J. Prost, *The Physics of Liquid Crystals*, Oxford Science Publications, 2nd edn, 1993.
- V. Koning, T. Lopez-Leon, A. Fernandez-Nieves and V. Vitelli, *Soft Matter*, 2013, **9**, 4993–5003.
- T. Lopez-Leon, A. Fernandez-Nieves, M. Nobili and C. Blanc, *Phys. Rev. Lett.*, 2011, **106**, 247802.
- J. Dzubiella, M. Schmidt and H. Löwen, *Phys. Rev. E: Stat. Phys., Plasmas, Fluids, Relat. Interdiscip. Top.*, 2000, **62**, 5081–5091.
- T. Lopez-Leon, V. Koning, K. B. S. Devaiah, V. Vitelli and A. Fernandez-Nieves, *Nat. Phys.*, 2011, **7**, 391–394.
- D. Zerrouki, B. Rotenberg, S. Abramson, J. Baudry, C. Goubault, F. Leal-Calderon, D. J. Pine and J. Bibette, *Langmuir*, 2006, **22**, 57–62.
- B. P. Binks, *Curr. Opin. Colloid Interface Sci.*, 2002, **7**, 21–41.
- S. Hernandez-Navarro, P. Tierno, J. Ignes-Mullol and F. Sagues, *Mol. Cryst. Liq. Cryst.*, 2015, **610**, 163–172.
- F. Smalenburg and H. Löwen, *J. Chem. Phys.*, 2016, **144**, 164903.
- E. Allahyarov, A. Voigt and H. Löwen, *Soft Matter*, 2017, **13**, 8120–8135.
- L. Onsager, *Ann. N. Y. Acad. Sci.*, 1949, **51**, 627–659.
- R. Wittmann, C. E. Sitta, F. Smalenburg and H. Löwen, *J. Chem. Phys.*, 2017, **147**, 134908.
- C. E. Sitta, F. Smalenburg, R. Wittkowski and H. Löwen, *Phys. Chem. Chem. Phys.*, 2018, **20**, 5285–5294.
- M. Schoen, T. Gruhn and D. J. Diestler, *J. Chem. Phys.*, 1998, **109**, 301–311.
- J.-P. Vest, G. Tarjus and P. Viot, 2018, arXiv:1803.00496, 1–15.
- N. D. Bade, R. Kamien, R. Assoian and K. Stebe, *Biophys. J.*, 2017, **112**(Supplement 1), 536a.

- 42 T. Geigenfeind, S. Rosenzweig, M. Schmidt and D. de las Heras, *J. Chem. Phys.*, 2015, **142**, 174701.
- 43 D. Matsunaga, F. Meng, A. Zöttl, R. Golestanian and J. M. Yeomans, *Phys. Rev. Lett.*, 2017, **119**, 198002.
- 44 R. Sknepnek and S. Henkes, *Phys. Rev. E: Stat., Nonlinear, Soft Matter Phys.*, 2015, **91**, 022306.
- 45 Y. Fily, A. Baskaran and M. F. Hagan, 2016, arXiv:1601.00324, 1–9.
- 46 S. Henkes, M. C. Marchetti and R. Sknepnek, 2017, arXiv:1705.05166, 1–13.
- 47 L. M. C. Janssen, A. Kaiser and H. Löwen, *Sci. Rep.*, 2017, **7**, 5667.
- 48 S. Shankar, M. J. Bowick and M. C. Marchetti, *Phys. Rev. X*, 2017, **7**, 031039.
- 49 A. Fernandez-Nieves, V. Vitelli, A. S. Utada, D. R. Link, M. Marquez, D. R. Nelson and D. A. Weitz, *Phys. Rev. Lett.*, 2007, **99**, 157801.
- 50 T. Lopez-Leon and A. Fernandez-Nieves, *Colloid Polym. Sci.*, 2011, **289**, 345–359.
- 51 H. L. Liang, J. Noh, R. Zentel, P. Rudquist and J. P. F. Lagerwall, *Philos. Trans. R. Soc., A*, 2013, **371**, 20120258.
- 52 H. L. Liang, S. Schymura, P. Rudquist and J. Lagerwall, *Phys. Rev. Lett.*, 2011, **106**, 247801.
- 53 R. Stannarius and K. Harth, *Phys. Rev. Lett.*, 2016, **117**, 157801.
- 54 S. Dölle and R. Stannarius, *Langmuir*, 2015, **31**, 6479–6486.
- 55 J. P. F. Lagerwall, C. Schütz, M. Salajkova, J. H. Noh, J. H. Park, G. Scalia and L. Bergström, *NSA Asia Mater.*, 2014, **6**, e80.
- 56 L. Jia, A. Cao, D. Lévy, B. Xu, P.-A. Albouy, X. Xiangjun, M. J. Bowick and M.-H. Li, *Soft Matter*, 2009, **5**, 3446–3451.
- 57 B. Xu, R. Piñol, M. Nono-Djamen, S. Pensec, P. Keller, P.-A. Albouy, D. Lévy and M.-H. Li, *Faraday Discuss.*, 2009, **143**, 235–250.
- 58 L. Jia, D. Lévy, D. Durand, M. Imperor-Clerc, A. Cao and M.-H. Li, *Soft Matter*, 2011, **7**, 7395–7403.
- 59 K. Stratford, R. Adhikari, I. Pagonabarraga, J. C. Desplat and M. E. Cates, *Science*, 2005, **309**, 2198–2201.
- 60 E. G. Kim, K. Stratford, P. S. Clegg and M. E. Cates, *Phys. Rev. E: Stat., Nonlinear, Soft Matter Phys.*, 2012, **85**, 020403.
- 61 W. Zhou, J. Cao, W. Liu and S. Stoyanov, *Angew. Chem., Int. Ed.*, 2009, **48**, 378–381.
- 62 S. V. Daware and M. G. Basavaraj, *Langmuir*, 2015, **31**, 6649–6654.
- 63 F. Lou, L. Ye, M. Kong, Q. Yang, G. Lia and Y. Huang, *RSC Adv.*, 2016, **6**, 24195–24202.
- 64 L. Ye, T. Zhou and X. Shen, *Mol. Imprinting*, 2015, **3**, 8–16.
- 65 L. B. G. Cortes, Y. Gao, R. P. A. Dullens and D. G. A. L. Aarts, *J. Phys.: Condens. Matter*, 2017, **29**, 064003.
- 66 A. H. Lewis, D. G. A. L. Aarts, P. D. Howell and A. Majumdar, *Stud. Appl. Math.*, 2017, **138**, 438–466.
- 67 Z. Yang, J. Wei, Y. I. Sobolev and B. A. Grzybowski, *Nature*, 2018, **553**, 313–318.
- 68 I. B. Liu, N. Sharifi-Mood and K. J. Stebe, *Annu. Rev. Condens. Matter Phys.*, 2018, **9**, 283–305.
- 69 S. J. Streichan, M. F. Lefebvre, N. Noll, E. F. Wieschaus and B. I. Shraiman, 2017, arXiv:1701.07100, 1–8.
- 70 C. Vega and S. Lago, *Comput. Chem.*, 1994, **18**, 55–59.